THz-driven surface plasmon undulator as a compact highly directional narrow band incoherent x-ray source

D. Rohrbach[1,*] C. B. Schroeder,[2] A. Pizzi,[1,†] R. Tarkeshian,[1,3] M. Hayati,[1]
W. P. Leemans,[4] and T. Feurer[1]

[1]*University of Bern, 3012 Bern, Switzerland*
[2]*Lawrence Berkeley National Laboratory, Berkeley, California 94720, USA*
[3]*European Spallation Source ERIC, 221 00 Lund, Sweden*
[4]*Deutsches Elektronen-Synchrotron (DESY), 22607 Hamburg, Germany*

We propose a short period undulator which is based on the alternating electromagnetic field pattern of THz-driven surface plasmons in a thin conductive layer on a dielectric grating. An approximate analytical model allows to assess the key performance parameters of the undulator and to estimate the emitted radiation spectrum. The specific example of a graphene based undulator is simulated in detail. For a moderate electron beam energy of 100 MeV and a bunch charge of 0.5 pC the 40 mm long undulator is shown to emit narrow band 1 keV x-ray pulses with a peak brightness of approximately 10^{16} photons/(s mrad^2 mm^2 0.1% BW). It therefore has potential for a compact and low cost x-ray source.

I. INTRODUCTION

In a variety of electron accelerator based light sources relativistic electron bunches propagate through an undulator and emit intense narrow band radiation [1–3]. Undulators are generally composed of a periodic, alternating array of normal-conducting or superconducting electromagnets, permanent magnets or hybrid magnets and the resulting magnetostatic field pattern forces the electrons on a wiggling orbit, which leads to emission of electromagnetic radiation [4]. Depending on the kinetic energy of the electrons and on the undulator period, the emission can range from THz to hard x-ray photon energies. Typical undulator periods are tens of millimeters, magnetic field strengths range from about one Tesla to more than ten Tesla for superconducting magnets, and undulators in free electron lasers can be tens to hundreds of meters in length [5,6].

In order to miniaturize undulators and/or to produce a given photon energy with less energetic electrons, the undulator period should be reduced. For example, the same photon energy can be achieved by a 10 times less energetic electron beam if the undulator period is reduced a

hundred-fold. Likewise, for a given electron energy the photon energy increases when the undulator period is reduced. A smaller scale undulator would also be beneficial for the development of compact light sources, especially in combination with miniaturized accelerators, for example, with those based on laser wakefields in plasma [7], ultrashort laser pulses in free space [8] or those based on laser-driven dielectric structures [9]. In the past, several efforts to reduce the periodicity of static magnetic field patterns have been made and values as low as 15 mm [10–13] were achieved. Further reduction down to about 100 μm was realized with laser micromachined permanent magnets [14] or electromagnets [15]. The peak magnetic field in these devices was still as high as 0.7 T [16]. A conceptually different approach uses oscillating electromagnetic fields, for example, in laser irradiated dielectric gratings [17], laser-driven undulators [18], microwave undulators [19], plasma wave undulators [20–22] or surface plasmon polariton (SPP) undulators [23,24].

In view of device miniaturization, the SPP based undulator is especially interesting since periods as low as 10 nm have been predicted. However, one has to bear in mind that SPPs exist at a conductor-dielectric interface and decay exponentially away from the interface on a length scale that is similar to its wavelength. For this reason the choice of SPP wavelength is determined by the transverse size of the electron bunch and is further influenced by its emittance, the opening angle of the radiation cone and possible wakefields excited at the interfaces. Without loss of generality we hereafter consider electron bunches with a transverse size of several tens of microns which results in a
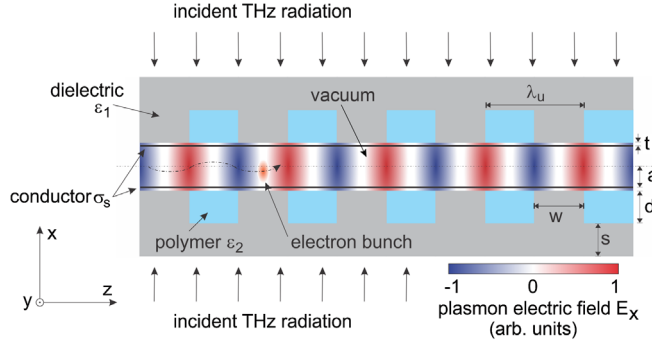

FIG. 1. Schematic of the THz-driven surface plasmon undulator. The incident THz radiations excite the SPPs via a dielectric grating. An electron bunch traveling through the vacuum channel interacts with the SPPs and emits high energy radiation.

SPP undulator driven by a THz to microwave range source depending on the SPP confinement factor, i.e., the ratio of SPP over free space wavelength. The SPP undulator with a gap size of several tens of microns has a period of approximately hundred microns, which is much shorter than it would be for a THz-driven dielectric grating undulator with a similar gap size [17].

II. SURFACE PLASMON UNDULATOR CONCEPT

A. Geometry

A schematic of the SPP undulator is shown in Fig. 1. It consists of two oppositely oriented dielectric gratings with periodicity λ_u and relative permittivity ϵ_1 which are separated by a gap of $2a$. The middle of the gap is at $x = 0$. Both gratings are coated with a thin conductive layer, which is characterized by an effective surface conductivity σ_s. The conductive layer can be a metal, a semiconductor or a two-dimensional material such as graphene. The latter case is considered in more detail in Sec. III. The grating grooves are filled with a low index polymer, with relative permittivity ϵ_2, to provide sufficient mechanical support for the conductive layer. The structure is excited by two counterpropagating and normally incident THz pulses ($\pm x$ axes) which are linearly polarized along the z axis. Their relative carrier phase difference is adjusted such that their electric fields cancel while their magnetic fields add at the center of the gap, i.e., at $x = 0$. The two THz pulses excite two counterpropagating SPPs ($\pm z$ axes) which, in case of spatial overlap, result in a standing wave pattern. At the center of the gap the SPPs are predominantly polarized normal to the grating-conductor interface, i.e., parallel to the x axis. The electron bunches propagate in the positive z direction and interact with the SPP fields and the THz drivers.

If the grating grooves are much longer in the y direction than the gap size, the problem reduces to two dimensions (xz plane) with transverse magnetic field distribution, i.e., $E_y = B_x = B_z = 0$.

B. Surface plasmons in a double-layer system

First we seek the resonance condition for efficient SPP excitation and approximate analytic expressions for the SPP fields in the structure. Approximating the two gratings by an effective medium with relative permittivity $\epsilon_e = \frac{w}{\lambda_u}\epsilon_1 + (1 - \frac{w}{\lambda_u})\epsilon_2$ (where w is the grating tooth width) results in the implicit SPP dispersion relation [25]

$$e^{2\kappa_v a}\left(\frac{\epsilon_e}{\kappa_e} + \frac{1}{\kappa_v} + \frac{i\sigma_s}{\epsilon_0\omega}\right)\left(\frac{1}{\kappa_v} + \frac{\epsilon_e}{\kappa_e} + \frac{i\sigma_s}{\epsilon_0\omega}\right)$$

$$= e^{-2\kappa_v a}\left(-\frac{\epsilon_e}{\kappa_e} + \frac{1}{\kappa_v} - \frac{i\sigma_s}{\epsilon_0\omega}\right)\left(\frac{1}{\kappa_v} - \frac{\epsilon_e}{\kappa_e} - \frac{i\sigma_s}{\epsilon_0\omega}\right), \quad (1)$$

with the frequency ω, the vacuum permittivity ϵ_0, $\kappa_v^2 = q^2 - \omega^2/c^2$, $\kappa_e^2 = q^2 - \epsilon_e\omega^2/c^2$, the SPP wave vector $q(\omega)$ and the speed of light in vacuum c. Efficient coupling of the incident THz radiation to the SPP, i.e., phase matching, requires $\Re(q(\omega)) = k_u$. From this condition and Eq. (1) the resonance frequency, ω_0, is found. The nonzero SPP fields at resonance are approximately given by

$$E_x = E_0 e^{-k_x a}\cosh(k_x x)(\cos\psi_- + \cos\psi_+),$$

$$E_z = E_0 e^{-k_x a}\frac{k_x}{k_u}\sinh(k_x x)(\sin\psi_- - \sin\psi_+),$$

$$B_y = E_0 e^{-k_x a}\frac{k_0}{ck_u}\cosh(k_x x)(\cos\psi_- - \cos\psi_+), \quad (2)$$

where E_0 is the electric field amplitude, $k_0 = 2\pi/\lambda_0 = \omega_0/c$ is the free space THz wave vector, $k_x^2 = k_u^2 - k_0^2$ and $\psi_\pm = \omega_0 t \pm k_u(z - z_0) - \pi/2$ are the phases of the two counter-propagating SPPs, where z_0 is the location of a grating edge. Here and hereafter the minus sign refers to the SPP copropagating with the electron bunch and the plus sign to the counterpropagating SPP. The fields experienced by an electron moving through the structure are a coherent super-position of the incident THz field and the SPP field. For simplicity we assume the THz field to be a plane wave with only one nonzero electric and magnetic field component which we hereafter refer to as E_{THz} and B_{THz}. The total fields then are

$$E_x \rightarrow E_x$$
$$E_z \rightarrow E_z + E_{\text{THz}}$$
$$B_y \rightarrow B_y + B_{\text{THz}}. \quad (3)$$

The relative SPP amplitude E_0/E_{THz} is determined by the absorption cross section and is extracted from numerical simulations. While the THz driver is typically a single cycle pulse, the resonant SPP fields oscillate for many cycles depending on the damping. Therefore, injecting electrons after the THz drivers have passed through the structure will eliminate their contribution and electrons will

interact with the SPP fields only. For the sake of completeness, we will consider SPPs as well as THz fields. The damping of the SPP fields can be neglected if one considers THz drivers with a tilted pulse front which is matched to the electron velocity [26–28].

C. Undulator radiation properties

We solve the relativistic Lorentz equation of motion for a single electron propagating through the fields given in Eq. (3) and characterize the emitted radiation by its wavelength, bandwidth and power. Unlike in undulators based on magnetostatic fields, the Lorentz factor γ is not a constant of motion since an electric field imparts energy on an electron. In the following we use the dimensionless on-axis SPP amplitude

$$a_u = \frac{eE_0}{mc^2 k_u} e^{-k_x a}, \tag{4}$$

where e is the elementary charge and m is the electron rest mass. For a typical SPP electric field strength and periodicity we find $a_u^2 \ll 1$. Therefore, we consider a series solution in powers of a_u and retain terms up to order $\mathcal{O}(a_u^2)$. The following further assumptions are used to solve the equation of motion: (i) $\beta_z \approx \beta_{z0} \gg \beta_x$, (ii) $\beta_{x0} \approx 0$, and (iii) $k_x x \approx 0$, where β_x and β_z are the x and z components of the electron velocity normalized to c, and β_{x0} and β_{z0} are the corresponding initial values. Within the series expansion, the radiation results from the oscillating electron velocity in the x direction, which is found to be

$$\beta_x = -\frac{1}{\gamma}(K^+ \sin\psi_+ - K^- \sin\psi_- + K_T \sin\psi_T), \tag{5}$$

with

$$\psi_\pm = \omega_0 t \pm k_u(\beta_{z0} ct - z_0) - \pi/2,$$
$$\psi_T = \omega_0 t + \varphi_T, \tag{6}$$

where $\beta_{ph} = k_0/k_u$ is the normalized phase velocity of the SPP fields and φ_T is the phase offset of the incident THz fields. $K^\pm$ and K_T are the undulator parameters for the copropagating and counterpropagating SPP and for the THz drivers, respectively. They are defined as

$$K^\pm = \frac{eE_0^\pm}{mc^2 \beta_{z0} k_u^\pm}$$
$$K_T = \frac{eE_T}{mc^2 \beta_{z0} k_T} \tag{7}$$

with the effective undulator wave vectors and associated effective field strengths

$$k_u^\pm = k_u\left(1 \pm \frac{\beta_{ph}}{\beta_{z0}}\right)$$
$$k_T = \frac{k_0}{\beta_{z0}}$$
$$E_0^\pm = E_0 e^{-k_x a}(1 \pm \beta_{ph}\beta_{z0})$$
$$E_T = 2\beta_{z0} E_{THz}. \tag{8}$$

For the highly relativistic case (i.e., $\gamma \gg 1$) we find that $K^\pm \approx a_u$ and that the three undulator wave vectors approach constant values, namely the free space THz wave vector k_T and the SPP wave vector k_u shifted by the phase velocities of the copropagating and the counterpropagating SPP. That is, the oscillating fields can be interpreted as a superposition of three electrostatic undulators each having a different effective periodicity and effective electric field strength.

Since in the frame moving at the initial electron speed the electron motion is nonrelativistic we may use the well-known Larmor equation to calculate the emitted radiation power:

$$P' = \frac{e^2}{6\pi\epsilon_0 c}\dot{\beta}'^2, \tag{9}$$

where primed variables refer to this moving frame and the dot indicates differentiation with respect to time.

By using $ct' = \gamma c(1 - \beta_{z0}^2)t$ the electron phase in the rest frame is found to be

$$\psi'_\pm = \frac{\omega_0 \pm k_u c\beta_{z0}}{\gamma(1 - \beta_{z0}^2)}t' \mp k_u z_0 - \frac{\pi}{2}. \tag{10}$$

The directional emission frequencies in the lab frame are obtained by considering the Doppler shift $\{\gamma[1 - \beta_{z0}\cos(\theta)]\}^{-1}$, where θ is the angle with respect to the propagation direction (z axis). The resulting emission frequencies and wavelengths are given by

$$\omega_r^\pm = \omega_0 \frac{\frac{\beta_{z0}}{\beta_{ph}} \pm 1}{1 - \beta_{z0}\cos(\theta)} \approx 2\gamma^2 c k_u^\pm$$
$$\lambda_r^\pm = \lambda_0 \frac{1 - \beta_{z0}\cos(\theta)}{\frac{\beta_{z0}}{\beta_{ph}} \pm 1} \approx \frac{\lambda_u^\pm}{2\gamma^2} \tag{11}$$

and similarly the emission wavelength due to the interaction with the THz drivers is given by

$$\lambda_r^T = \lambda_0[1 - \beta_{z0}\cos(\theta)] \approx \frac{\lambda_T}{2\gamma^2}, \tag{12}$$

where $\lambda_u^\pm = \frac{2\pi}{k_u^\pm}$ and $\lambda_T = \frac{2\pi}{k_T}$. The approximations hold for $\theta = 0$ and for highly relativistic electrons. Note that Eqs. (11) and (12) are similar to those found for a magnetic

undulator, where $\lambda_r = \frac{\lambda_u}{2\gamma^2}(1 + K^2/2)$ [29], assuming $K \ll 1$.

The emitted radiation is linearly polarized in the x direction and the total emitted energy can be estimated via Eq. (9). Using $\beta'_x = \gamma^2\beta_x$ and averaging over one undulator period one obtains the averaged emitted power $\bar{P}^{\pm}$ due to the interaction with the copropagating and counterpropagating components of the SPP:

$$\bar{P}^{\pm} = \frac{Qe\gamma^2 c\beta_{z0}^2}{12\pi\epsilon_0}(K^{\pm}k_u^{\pm})^2, \tag{13}$$

where Q is the bunch charge and where incoherent emission is assumed. A similar equation is obtained for the interaction with the THz drivers when $K^{\pm}$ and $k_u^{\pm}$ are replaced by the corresponding parameters. We obtain the emitted energy by multiplying the average power by the time of flight through the undulator $L/(c\beta_{z0})$,

$$W^{\pm} = \frac{LQe\gamma^2\beta_{z0}}{12\pi\epsilon_0}(K^{\pm}k_u^{\pm})^2, \tag{14}$$

which scales with the square of the electric field amplitude. The relative bandwidth of the emission mainly depends on the number of undulator periods and the relative energy spread of the electrons. The natural bandwidth of an undulator can be estimated by considering the Fourier transform limit of the radiation cycles [29]. At the central frequencies $\omega_r^{\pm}$, the emitted radiation oscillates $N_u^{\pm} = Lk_u^{\pm}/(2\pi)$ times resulting in a relative bandwidth

$$\frac{\Delta\omega_r^{\pm}}{\omega_r^{\pm}} = \sqrt{(0.886/N_u^{\pm})^2 + (2\Delta E/E)^2}, \tag{15}$$

where $\Delta\omega_r^{\pm}$ is the full width at half maximum (FWHM) of the on-axis spectral intensity and $\Delta E = 2\sqrt{2\ln 2}\sigma_E$ is the FWHM of the initial energy spread of the electrons (assuming a Gaussian energy distribution).

III. GRAPHENE SURFACE PLASMON UNDULATOR

We next study the explicit case of an SPP undulator with two monolayers of graphene as conductive sheet material. Graphene is well suited as a plasmonic material in the THz range [25] and exhibits a very high breakdown threshold, in excess of 3 GV/m for 50 fs pulses with a center wavelength of 790 nm [30]. To the best of our knowledge, there is no measurement of the graphene breakdown threshold in the THz range, but in the following we will assume a breakdown threshold exceeding 1 GV/m.

TABLE I. Proposed graphene SPP undulator parameters (see also Fig. 1 for the definition of parameters).

Parameter	Value
Undulator length L	40 mm
Gap height $2a$	50 μm
Grating periodicity λ_u	130 μm
Grating tooth width w	$\lambda_u/2$
Groove depth d	$\lambda_u/2$
Substrate thickness s	25 μm
Grating relative permittivity ϵ_1	3.9
Polymer relative permittivity ϵ_2	2.0
Grating—graphene distance t	0.5 μm
THz peak electric field E_{THz}	100 MV/m

A. Geometry

We numerically tested the SPP undulator with experimentally viable parameters. The grating period and the gap height are set to 130 and 50 μm, respectively, which are a good compromise to accommodate electron bunches with transverse sizes on the order of tens of microns while resulting in a close to homogeneous in-gap field distribution in the x direction. The undulator length is arbitrarily set to $L = 40$ mm (corresponding to 300 grating periods) but in practice is linked to the available THz source [31] as one has to maintain the desired field strength over the entire undulator length. We can estimate the needed THz energy assuming a tilted pulse front with a focal size of 40 mm by 300 μm, a pulse duration of 1 ps and a field strength of 100 MV/m. For these parameters the energy of the two THz drivers is approximately 0.3 mJ, which could be obtained by today's THz sources [32,33]. For the dielectric grating material we consider fused silica and for the polymer high-density polyethylene. Table I summarizes all the relevant dimensions of the graphene SPP undulator.

B. Graphene surface plasmon fields

We calculate the resonance condition and the SPP fields for the parameters listed in Table I using the finite-element software COMSOL Multiphysics [34]. The simulations were performed in two dimensions (xz plane), in the frequency domain and for at least one unit cell of the grating, using periodic and scattering boundary conditions in z and x directions, respectively. The graphene layers were modeled as surface current boundary conditions and their conductivity was described by a Drude-like expression [25] which is a reasonable approximation at room temperature and for THz frequencies,

$$\sigma_g(\omega) = \frac{\sigma_0}{\pi}\frac{4E_F}{\hbar/\tau - i\hbar\omega}, \tag{16}$$

with $\sigma_0 = e^2/(4\hbar)$, the Fermi energy E_F and the scattering time τ. A distinctive feature of graphene, which makes it an ideal candidate for the realization of the proposed undulator, is that the Fermi energy E_F and therefore the
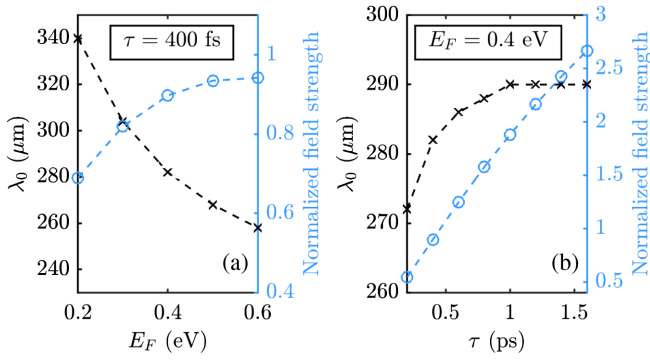
FIG. 2. Resonance wavelength λ_0 and normalized field strength E_x/E_{THz} at the center of the gap ($x = 0$) as a function of Fermi energy E_F (a) and relaxation time τ (b). The dashed lines serve as a guide to the eye.

conductivity can be tuned via doping or by applying a gate voltage. The scattering time τ is determined by the quality of the graphene layer and values between 400 fs and 1.6 ps have been reported [35]. Figure 2 shows the resonance wavelength λ_0 and the normalized field strength E_x/E_{THz} at the center of the gap for Fermi energies between 0.2 and 0.6 eV (for $\tau = 400$ fs) and for scattering times between 200 fs and 1.6 ps (for $E_F = 0.4$ eV).

Hereafter, we numerically test the undulator for $E_F = 0.4$ eV and $\tau = 400$ fs. The resulting THz absorption spectrum is shown in Fig. 3 (blue dashed curve) and reveals a resonance at 290 μm which agrees reasonably well with the analytic approximations (1). The maximum absorption is close to 50% indicating efficient coupling. The black solid curve shows the normalized field strength E_x/E_{THz} at the center of the gap. Interestingly, its maximum appears at a somewhat lower wavelength when compared to the absorption curve, i.e., at 282 μm. This difference is explained by the near-field diffraction pattern of the grating structure itself, which is more pronounced for shorter wavelengths and which adds to the total field distribution causing the observed redshift of the maximum. For a grating periodicity of 130 μm and a resonance free

space wavelength of 282 μm the normalized phase velocity is $\beta_{ph} = 0.46$.

Figure 4 shows the nonzero field components excited by two counterpropagating THz sources at the resonance wavelength $\lambda_0 = 282$ μm along four undulator periods. Recall that the fields are composed of the incident THz field and the SPP fields. The field components E_x and B_y are relatively homogeneous in the x direction within the gap, and E_z vanishes near the gap center where the electrons propagate.

Of special interest are the fields close to the gap center where the electrons propagate, which we show in Fig. 5 as a function of z along four undulator periods.

We now calculate the effective undulator parameter as defined in Eq. (7). Figure 6 shows $K^\pm$ versus kinetic energy for two different SPP field strengths $E_0 = 100$ MV/m (a) and $E_0 = 1$ GV/m (b).

For relativistic energies the $K^\pm$ parameters approach the same asymptotic value which depends linearly on the SPP field strength (e.g., $K^\pm = 0.014$ for a field strength of 1 GV/m). The undulator parameter is limited by the breakdown threshold of graphene and the available THz source. For comparison, a typical magnetic undulator has $K \approx 1$ [36]. Consequently we expect a lower spectral intensity of the emitted radiation.

FIG. 4. Color-coded SPP field distributions in the xz plane. The SPPs are excited by two THz drivers counterpropagating in the $\pm x$ direction and the fields are normalized to the THz field strength. Top: x-component of the electric field; middle: z-component of the electric field; bottom: y-component of the magnetic field.
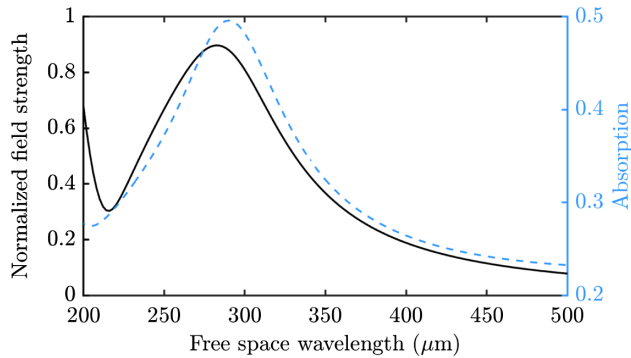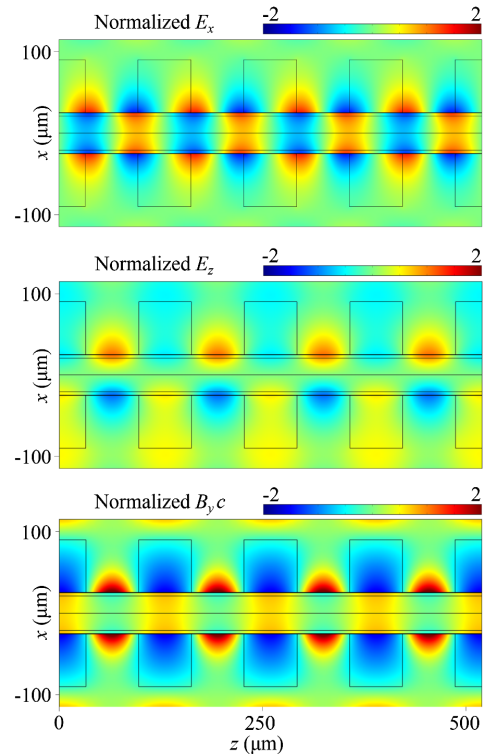

FIG. 3. Simulated absorption (blue dashed curve) and normalized field strength E_x/E_{THz} at the center of the gap (black solid curve) versus wavelength.
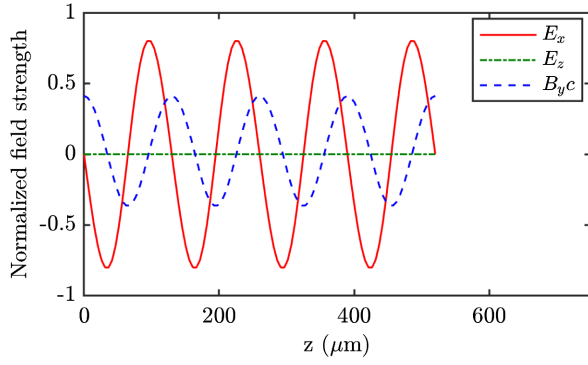
FIG. 5.   Simulated field components along the center of the gap as a function of the distance z. The field amplitudes are normalized to the incident THz field strength.
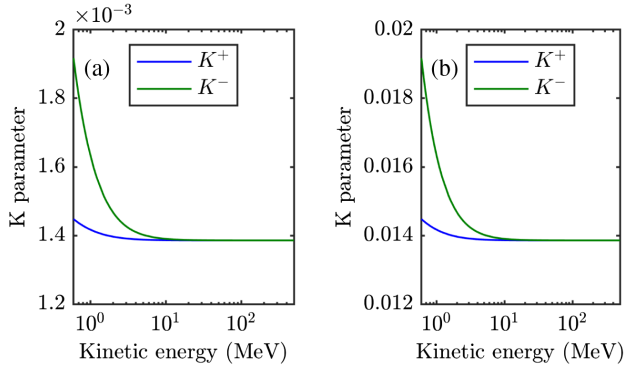

FIG. 6. K parameters versus kinetic energy calculated from Eq. (7) for a plasmon electric field strength of 100 MV/m (a) and 1 GV/m (b).

C. Electron bunches

The electron trajectories were calculated with VDSR [37] based on the field maps from the COMSOL simulation. A fourth order Runge-Kutta method was used where particle interactions were neglected, which is justified by the relativistic beam energies and the short undulator length [23]. In order to verify the assumption of negligible particle interactions we simulated the drift of an electron bunch with parameters as given in Table II in CST [38] taking into account particle interactions. We found that the transverse beam size increases by only 10% and therefore still matches the gap height. Based on the trajectories we calculated the intensity of the emitted radiation per frequency interval and per solid angle in the far field based on [39]

$$\frac{\mathrm{d}^2 I}{\mathrm{d}\omega \mathrm{d}\Omega} = \frac{e^2}{16\pi^3 \varepsilon_0 c}$$

$$\times \left| \int_{-\infty}^{\infty} \frac{\hat{\mathbf{n}}_r \times [(\hat{\mathbf{n}}_r - \beta) \times \dot{\beta}]}{(1 - \hat{\mathbf{n}}_r \beta)^2} \exp\left(i\omega\left(t - \frac{\hat{\mathbf{n}}_r \mathbf{r}}{c}\right)\right) \mathrm{d}t \right|^2,$$

(17)

where $\hat{\mathbf{n}}_r$ is the unit vector pointing in the observation direction. The radiation spectra generated by an electron

TABLE II.   Parameters for numerical simulations.

Parameter	Value
Kinetic energy E	100 MeV
Relative energy spread σ_E/E	0.02%
Bunch charge Q	0.5 pC
Transverse size σ_r	5 μm
Longitudinal size σ_z	5 μm

bunch was calculated by incoherently adding all spectra of the 5000 macroparticles, which were used for representing the bunch. The simulation parameters, unless stated otherwise, are summarized in Table II.

The kinetic energy was fixed to 100 MeV and we assumed a relative energy spread of 0.02%, as provided by today's accelerators [5]. The electron bunch in the lab frame had a Gaussian charge distribution with standard deviations σ_r and σ_z in transverse and longitudinal directions. For simplicity, we set the emittance to zero, that is, the electrons have no initial momentum in the x and y directions. If required, the maximum allowed emittance can be estimated by setting the maximum transverse bunch size equal to the gap size and by using a beta function determined by the undulator length L. As a result, the geometric emittance must be much smaller than $a^2/L = 15.6$ nm rad which corresponds to a normalized emittance of 3.1 μm rad.

Before we discuss the undulator performance, we estimate the magnitude of possible wakefields excited by the electrons. Wakefields will not only modify the undulator field pattern and thus the undulator performance, but also lead to an energy loss of the electrons on their passage through the undulator. We simulated wakefields using CST [38]. For simplicity we approximate the electron bunch by a line current with a longitudinal Gaussian distribution with standard deviation σ_z. We then calculate the energy loss of a virtual spectator electron that follows the bunch at a variable distance. Figure 7 shows the wake potential for two different cases, i.e., for σ_z equal to 5 and 10 microns. The maximum wake potential amplitude for $\sigma_z = 5$ μm is as high as 540 kV/pC. The wake potential could be further reduced by defocusing the bunch in the y direction and therefore decrease the charge density.

In order to reduce the relative energy loss for a 100 MeV beam, a small bunch charge of 0.5 pC is considered. That is, the relative energy loss is approximately 0.3% and will be neglected in the following.

D. Undulator performance

Unlike magnetic undulators where the alternating magnetic field pattern is time independent, THz driven SPP fields oscillate while the electrons propagate through the structure. Therefore the time delay between the electron injection and the THz driver determines the average
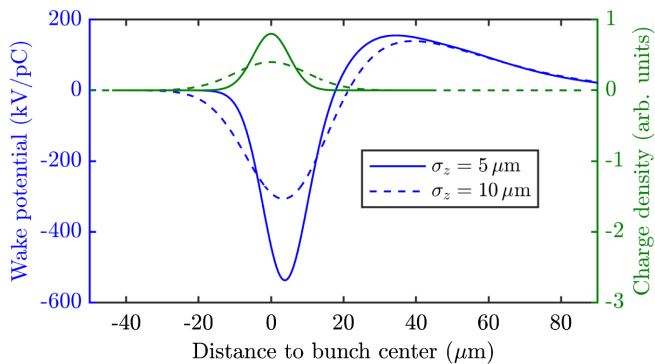
FIG. 7. Simulated wake potential normalized to the bunch charge as a function of distance to the bunch center (negative values refer to positions at the bunch front). Two different bunch lengths with $\sigma_z = 5 \ \mu$m (solid lines) and $\sigma_z = 10 \ \mu$m (dashed lines) are considered.

electron velocity in the x direction, which in turn leads to an overall deflection in the x direction. Figure 8 shows the overall deflection Δx at the end of the undulator versus the time delay between THz drivers and electron injection.

An electron injected at zero time delay, or at integer multiples of half the THz oscillation period, will perform a wiggling motion on its passage through the undulator but will not experience a net deflection at the end of the undulator. If injected a quarter oscillation before or after, the net deflection can be as large as the gap size and electrons might collide with the graphene. Moreover, the emission cone bends away from the z axis. In the following we assume that electron bunches are injected so that their center of charge in the longitudinal direction has a zero time delay.

Next, we consider the x component of the normalized momentum of a single electron during its passage through the undulator as it is shown in Fig. 9(a) for a field strength of 100 MV/m and a kinetic energy of 100 MeV.

We observe a complex beating pattern, which is characterized by Fourier peaks at 22, 26, and 71 mm^{-1} as shown in Fig. 9(b). As discussed in Eq. (8) the three peaks originate from electrons interacting with the incident THz

FIG. 9. Simulated x component of the normalized momentum of a single electron along its passage through the undulator (a) and the corresponding Fourier transformation with peaks at wave vectors of 22, 26, and 71 mm^{-1} (b), where the dashed lines correspond to the analytical predictions of Eq. (8).

fields (k_T) and the copropagating and counterpropagating SPP fields ($k_u^{\pm}$). The analytical predictions of the effective undulator wave vectors, shown as dashed lines, agree with the simulation results, while the predicted undulator parameters of Eq. (7) agree with the ratio of the peak amplitudes. Accordingly, we expect several emission peaks in the emitted radiation spectrum.

Figure 10 shows the emission wavelength versus kinetic energy and we find good agreement between simulation results and analytical predictions based on Eq. (11) as long as the THz electric field strength is not higher than approximately 100 MV/m.
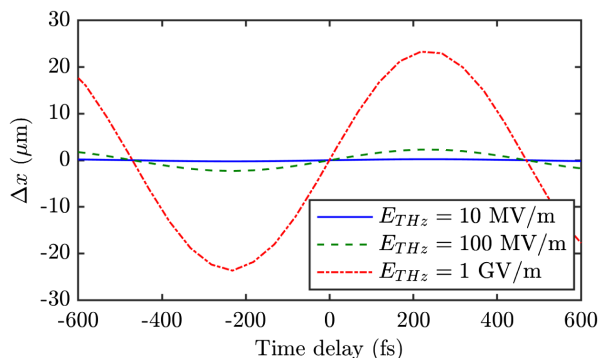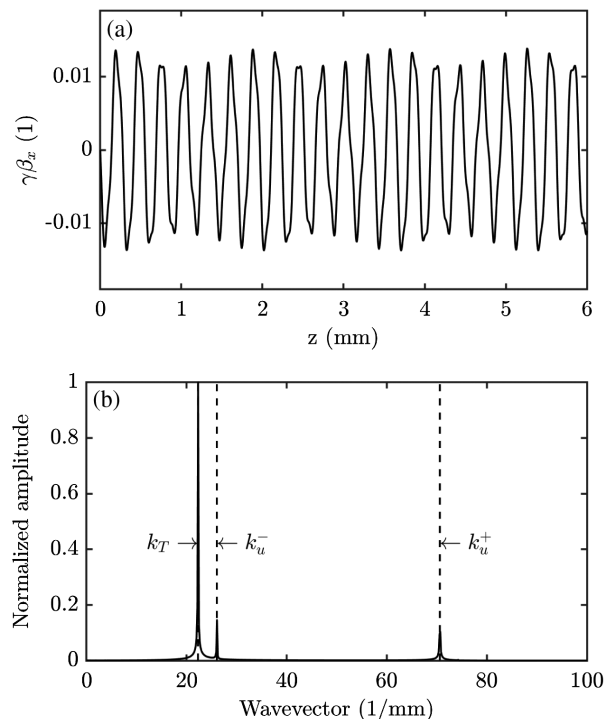

FIG. 8. Simulated overall deflection of the electrons in the x direction as a function of the time delay between the THz drivers and the electron injection for different field strength E_{THz}.
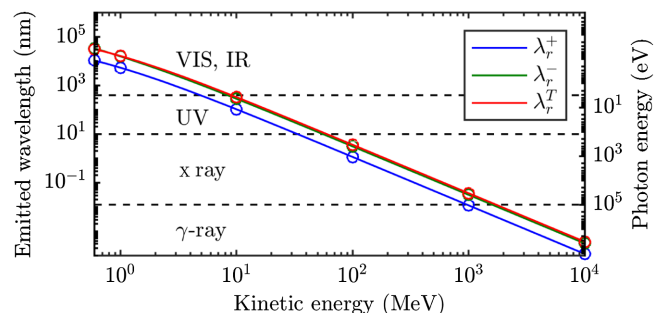

FIG. 10. Emission wavelengths versus kinetic energy calculated from Eq. (11) (solid curves) and from numerical simulations (circles) with $E_{\text{THz}} = 100$ MV/m.
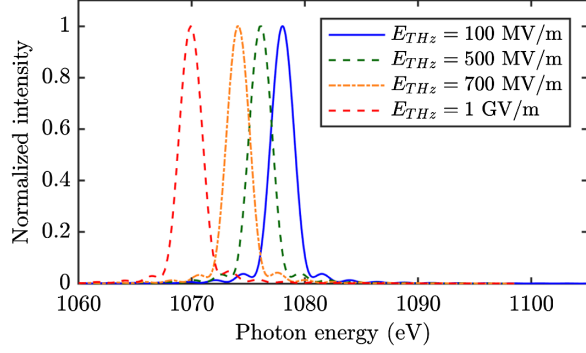
FIG. 11. Normalized on-axis spectrum from numerical simulations for a THz-field strength of 100 MV/m (blue curve), 500 MV/m (green curve), 700 MV/m (orange curve) and 1 GV/m (red curve).

For a moderate kinetic energy of 600 keV the emission wavelengths are on the order of tens of microns and for increasing kinetic energies they decrease following a power law of approximately E^{-2}. Note that for low beam energies the electron bunch might collapse due to wakefield coupling and Coulomb repulsion, therefore these values are limited to low bunch charges. At kinetic energies as high as 1 GeV the photon energy approaches 100 keV.

For SPP field strengths in excess of 100 MV/m the emission peaks start to deviate from the analytic prediction (11) as shown in Fig. 11 for the $\hbar\omega_r^+$ emission. Such redshift is also found in magnetic undulators when the undulator parameter is increased and results from the decreased average velocity in the z direction [29]. In the following we always consider a THz field strength of 100 MV/m.

As mentioned above, the emission can be tuned by changing the graphene conductivity. For instance, lowering the Fermi energy to 0.2 eV shifts the resonance wavelength from $\lambda_0 = 282\ \mu$m to $\lambda_0 = 340\ \mu$m. This in turn alters the SPP phase velocity β_{ph} and the $\hbar\omega_r^+$ emission energy decreases from 1078 to 1020 eV, that is by 5%.

From the emitted energy $W^\pm$ per bunch, i.e., Eq. (14), we can estimate the brightness B, which is the radiation flux divided by the phase space volume. We assume that the photon bunch duration is equal to the electron bunch duration and the transverse size of the photon beam is determined by the electron beam, such that $\sigma_\gamma = \sigma_r$. From numerical simulation we find a peak intensity of 5.5×10^5 photons/(sr 0.1% BW) which corresponds to a peak brightness of $B = 10^{16}$ photons/(s mrad^2 mm^2 0.1% BW). Note that the peak intensity is proportional to E_{THz}^2 and also to E^2. Therefore the brightness can be increased by higher THz field strengths and/or higher electron beam energies.

Next, we analyze the angular distribution of the emitted radiation for the highest photon energy peak $\hbar\omega_r^+$ (similar results are found for the other emission
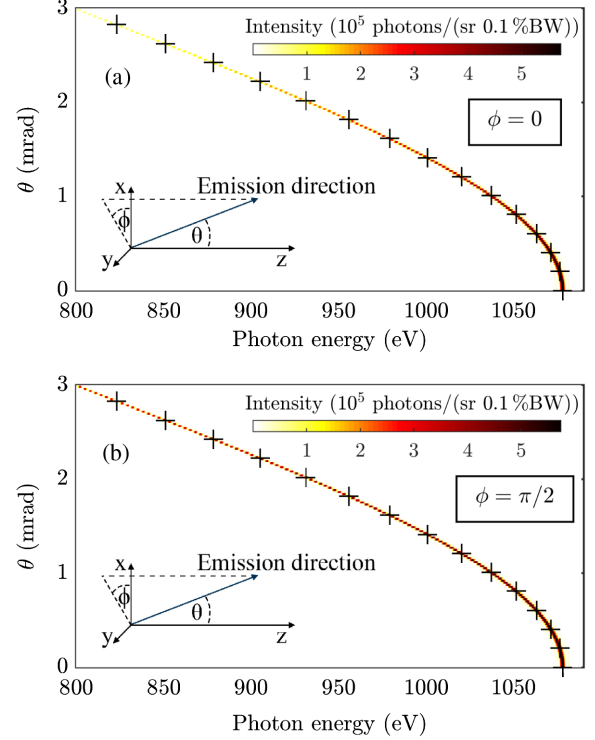

FIG. 12. Angular dependence of photon energy and intensity (color coded) in the xz plane (a) and in the yz plane (b) from numerical simulations. The black crosses correspond to the analytical results from Eq. (11).

peaks). Figure 12 shows a color-coded map of the emission intensity versus polar angle θ and photon energy for two different values of ϕ. The black crosses mark the analytical results from Eq. (11).

The highest photon energy and emission intensity are observed on axis ($\theta = 0$). Moreover we find a slight anisotropy in emission due to the undulator motion in the polarization plane, that is, the intensity decays slightly slower with polar angle in the yz plane as compared to the xz plane.

Finally, we study the natural bandwidth of the emission peaks and investigate further broadening mechanisms. Here, we find a natural relative bandwidth of 0.2%. This is further affected by relative energy spread of the electron bunch. Figure 13 depicts the influence of the electron beam's energy spread on the relative bandwidth of the on-axis spectrum. While the peak intensity decreases with increasing energy spread the bandwidth grows, which is in qualitative agreement with Eq. (15).

Lastly, we analyze the influence of longitudinal bunch size σ_z and transverse bunch size σ_r on the radiation spectrum. We found that both the on-axis intensity and bandwidth are independent of the longitudinal bunch size. When varying the transverse bunch size one has to keep in mind that the maximum bunch size is limited by the gap between the two graphene layers (here 50 μm). Therefore the considered transverse bunch size is always smaller than
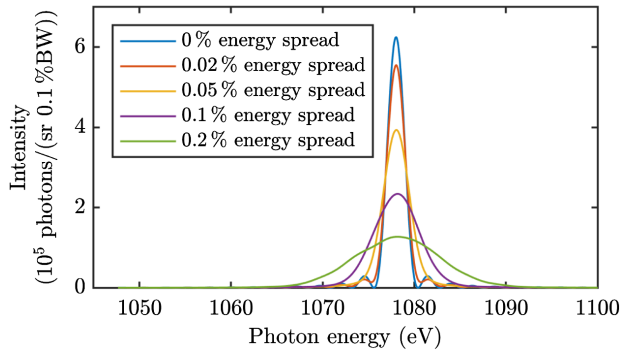
FIG. 13. Simulated on-axis spectrum for electron beams with energy spreads of 0%, 0.02%, 0.05%, 0.1% and 0.2%.

the plasmon extent (i.e., $k_x \sigma_r < 0.5$). While the bandwidth remains unaffected the intensity increases with transverse bunch size. This is explained by the fact that a larger transverse beam comes closer to the graphene layers and those parts of the electron bunch experience a higher SPP field strength with the consequence of a slightly higher intensity.

IV. CONCLUSIONS

Propagating a 0.5 pC electron bunch with a kinetic energy of 100 MeV through a 40 mm long undulator with a periodicity of 130 μm and driven by a state-of-the-art THz source was shown to emit x rays with photon energies around 1 keV and a peak brightness of approximately 10^{16} photons/(s mrad^2 mm^2 0.1% BW). The emission spectrum consists of three peaks which result from inter-action with two counterpropagating plasmon fields and THz driver. The proposed THz driven SPP undulator may pave the way to a low cost, compact and tunable radiation source, which produces highly directional, linearly polar-ized and narrow band x-ray pulses. Without question, the SPP undulator cannot compete with undulators used in free electron lasers, however, such compact sources may find applications in radiotherapy, ultrafast x-ray diffraction experiments or time-resolved x-ray spectroscopy. Its bright-ness is similar, for example, to that of electron slicing sources [40–42].

As an outlook, there are several avenues along which the THz-driven undulator performance could be optimized, i.e., a higher K parameter, a smaller device structure or a gamma photon source.

First, the K parameter of 0.014 could be pushed closer towards one and therefore closer to parameters found for standard magnetic undulators. Since the K parameter scales linearly both with electric field strength and undulator periodicity two options arise, either to increase the electric field strength or the periodicity by a factor of about 70. Increasing the periodicity is certainly possible but would be detrimental in view of device miniaturization. A 70-fold higher THz field strength (around 70 GV/m) may exceed

the material damage threshold. Nevertheless, 10 GV/m should be feasible and together with a larger periodicity of 1 mm should result in a K parameter close to one.

Second, to miniaturize the device even further would go hand in hand with a smaller periodicity which is feasible for highly focused and low emittance electron beams. A smaller period would further reduce the kinetic energy requirement for producing a fixed x-ray photon energy. The extreme case of a ten nanometer period was demonstrated by Wong and co-workers [23].

Third, optimizing the device for a 5 GeV electron beam would result in the production of 2.5 MeV photons and therefore the SPP undulator might be an interesting source for gamma spectroscopy.

[1] C. Pellegrini, A. Marinelli, and S. Reiche, The physics of x-ray free-electron lasers, Rev. Mod. Phys. **88,** 015006 (2016).

[2] J. M. J. Madey, Stimulated emission of bremsstrahlung in a periodic magnetic field, J. Appl. Phys. **42,** 1906 (1971).

[3] D. A. G. Deacon, L. R. Elias, J. M. J. Madey, G. J. Ramian, H. A. Schwettman, and T. I. Smith, First Operation of a Free-Electron Laser, Phys. Rev. Lett. **38,** 892 (1977).

[4] J. A. Clarke, *The Science and Technology of Undulators and Wigglers* (Oxford University Press, New York, 2004), https://www.oxfordscholarship.com/view/10.1093/acprof: oso/9780198508557.001.0001/acprof-9780198508557.

[5] V. S. Paul Scherrer Institute (PSI), SwissFEL—Conceptual design report, Technical Report, 2010, https://inis.iaea.org/ search/search.aspx?orig_q=RN:42006326.

[6] LCLS Parameters, https://portal.slac.stanford.edu/sites/ lclscore_public/ Accelerator_Physics_Published_Documents/LCLS-parameters-3-22-17.pdf.

[7] E. Esarey, C. B. Schroeder, and W. P. Leemans, Physics of laser-driven plasma-based electron accelerators, Rev. Mod. Phys. **81,** 1229 (2009).

[8] L. J. Wong, K.-H. Hong, S. Carbajo, A. Fallahi, P. Piot, and M. Soljačić, J. D. Joannopoulos, F. X. Kärtner, and I. Kaminer, Laser-induced linear-field particle acceleration in free space, Sci. Rep. **7,** 11159 (2017).

[9] R. J. England *et al.*, Dielectric laser accelerators, Rev. Mod. Phys. **86,** 1337 (2014).

[10] J.-C. Huang, H. Kitamura, C.-K. Yang, C.-H. Chang, C.-H. Chang, and C.-S. Hwang, Challenges of in-vacuum and cryogenic permanent magnet undulator technologies, Phys. Rev. Accel. Beams **20,** 064801 (2017).

[11] H. Hsieh, S. Krinsky, A. Luccio, C. Pellegrini, and A. Van Steenbergen, Wiggler, undulator and free electron laser

radiation sources development at the national synchrotron light source, Nucl. Instrum. Methods **208**, 79 (1983).

[12] W. Gudat, J. Pflüger, J. Chatzipetros, and W. Peatman, An undulator/multipole wiggler for the bessy storage ring, Nucl. Instrum. Methods **246**, 50 (1986).

[13] S. Yamamoto, T. Shioya, M. Hara, H. Kitamura, X. W. Zhang, T. Mochizuki, H. Sugiyama, and M. Ando, Construction of an in-vacuum type undulator for production of undulator x rays in the 5–25 keV region, Rev. Sci. Instrum. **63**, 400 (1992).

[14] B. A. Peterson, O. D. Oniku, W. C. Patterson, D. Le Roy, A. Garraud, F. Herrault, N. M. Dempsey, D. P. Arnold, and M. G. Allen, Technology development for short-period magnetic undulators, Phys. Procedia **52**, 36 (2014).

[15] J. Harrison, A. Joshi, Y. Hwang, O. Paydar, J. Lake, P. Musumeci, and R. N. Candler, Surface-micromachined electromagnets for 100 μm-scale undulators and focusing optics, Phys. Procedia **52**, 19 (2014).

[16] J. Harrison, A. Joshi, J. Lake, R. Candler, and P. Musumeci, Surface-micromachined magnetic undulator with period length between 10 μm and 1 mm for advanced light sources, Phys. Rev. ST Accel. Beams **15**, 070703 (2012).

[17] T. Plettner and R. L. Byer, Proposed dielectric-based microstructure laser-driven undulator, Phys. Rev. ST Accel. Beams **11**, 030704 (2008).

[18] F. Toufexis, T. Tang, and S. Tantawi, A 200 μm-period laser-driven undulator, in *Proceedings of the 36th International Free Electron laser Conference, Basel, 2014* (Paul Scherrer Institute (PSI), 2014), ISBN: 978-3-95450-133-5, http://accelconf.web.cern.ch/AccelConf/FEL2014/papers/mop047.pdf.

[19] S. Tantawi, M. Shumail, J. Neilson, G. Bowden, C. Chang, E. Hemsing, and M. Dunning, Experimental Demonstration of a Tunable Microwave Undulator, Phys. Rev. Lett. **112**, 164802 (2014).

[20] S. Corde and K. Ta Phuoc, Plasma wave undulator for laser-accelerated electrons, Phys. Plasmas **18**, 033111 (2011).

[21] R. L. Williams, C. E. Clayton, C. Joshi, and T. C. Katsouleas, Studies of classical radiation emission from plasma wave undulators, IEEE Trans. Plasma Sci. **21**, 156 (1993).

[22] S. G. Rykovanov, C. B. Schroeder, E. Esarey, C. G. R. Geddes, and W. P. Leemans, Plasma Undulator Based on Laser Excitation of Wakefields in a Plasma Channel, Phys. Rev. Lett. **114**, 145003 (2015).

[23] L. J. Wong, I. Kaminer, O. Ilic, J. D. Joannopoulos, and M. Soljačić, Towards graphene plasmon-based free-electron infrared to x-ray sources, Nat. Photonics **10**, 46 (2016).

[24] G. Rosolen, L. J. Wong, N. Rivera, B. Maes, and M. Soljačić, and I. Kaminer, Metasurface-based multiharmonic free-electron light source, Light: Sci. Appl. **7**, 64 (2018).

[25] P. A. D. Gonçalves and N. M. R. Peres, *An Introduction to Graphene Plasmonics* (World Scientific, Singapore, 2015), p. 464, https://www.worldscientific.com/worldscibooks/10.1142/9948.

[26] T. Feurer, J. C. Vaughan, and K. A. Nelson, Spatiotemporal coherent control of lattice vibrational waves, Science **299**, 374 (2003).

[27] S. Akturk, X. Gu, E. Zeek, and R. Trebino, Pulse-front tilt caused by spatial and temporal chirp, Opt. Express **12**, 4399 (2004).

[28] L. J. Wong and I. Kaminer, Ultrashort tilted-pulse-front pulses and nonparaxial tilted-phase-front beams, ACS Photonics **4**, 2257 (2017).

[29] P. Schmüser, M. Dohlus, J. Rossbach, and C. Behrens, *Free-Electron Lasers in the Ultraviolet and X-Ray Regime* (Springer International Publishing, Cham, Heidelberg, New York, Dordrecht, London, 2014), https://doi.org/10.1007/978-3-319-04081-3.

[30] A. Roberts, D. Cormode, C. Reynolds, T. Newhouse-Illige, B. J. LeRoy, and A. S. Sandhu, Response of graphene to femtosecond high-intensity laser irradiation, Appl. Phys. Lett. **99**, 051912 (2011).

[31] H. A. Hafez, X. Chai, A. Ibrahim, S. Mondal, D. Férachou, X. Ropagnol, and T. Ozaki, Intense terahertz radiation and their applications, J. Opt. **18**, 093004 (2016).

[32] L. Wang, A. Fallahi, K. Ravi, and F. Kärtner, High efficiency terahertz generation in a multistage system, Opt. Express **26**, 29744 (2018).

[33] F. Ahr, S. W. Jolly, N. H. Matlis, S. Carbajo, T. Kroh, K. Ravi, D. N. Schimpf, J. Schulte, H. Ishizuki, T. Taira, A. R. Maier, and F. X. Kärtner, Narrowband terahertz generation with chirped-and-delayed laser pulses in periodically poled lithium niobate, Opt. Lett. **42**, 2118 (2017).

[34] COMSOL MULTIPHYSICS, https://www.comsol.com (2019).

[35] A. Woessner, M. B. Lundeberg, Y. Gao, A. Principi, P. Alonso-González, M. Carrega, K. Watanabe, T. Taniguchi, G. Vignale, M. Polini, J. Hone, R. Hillenbrand, and F. H. L. Koppens, Highly confined low-loss plasmons in graphene-boron nitride heterostructures, Nat. Mater. **14**, 421 (2015).

[36] C. J. Milne *et al.*, *SwissFEL: The Swiss X-ray Free Electron Laser* (2017), Vol. 7, p. 720, https://doi.org/10.3390/app7070720.

[37] M. Chen, E. Esarey, C. G. R. Geddes, C. B. Schroeder, G. R. Plateau, S. S. Bulanov, S. Rykovanov, and W. P. Leemans, Modeling classical and quantum radiation from laser-plasma accelerators, Phys. Rev. ST Accel. Beams **16**, 030701 (2013).

[38] CST—Computer Simulation Technology, https://www.cst.com (2019).

[39] J. D. Jackson, *Classical Electrodynamics*, 3rd ed. (Wiley, New York, 1999), http://cdsweb.cern.ch/record/490457.

[40] A. A. Zholents and M. S. Zolotorev, Femtosecond X-ray Pulses of Synchrotron Radiation, Phys. Rev. Lett. **76**, 912 (1996).

[41] R. W. Schoenlein, S. Chattopadhyay, H. H. W. Chong, T. E. Glover, P. A. Heimann, C. V. Shank, A. A. Zholents, and M. S. Zolotorev, Generation of femtosecond pulses of synchrotron radiation, Science **287**, 2237 (2000).

[42] G. Ingold, A. Streun, B. Singh, R. Abela, P. Beaud, G. Knopp, L. Rivkin, V. Schlott, T. Schmidt, H. Sigg, J. F. van der Veen, A. Wrulich, and S. Khan, Subpicosecond optical pulses at the SLS storage ring, in *Proceedings of the 19th Particle Accelerator Conference, Chicago, IL, 2001* (IEEE, Piscataway, NJ, 2001), Vol. 4, pp. 2656–2658, https://ieeexplore.ieee.org/document/987863.